

# On the source of the Fe $K\alpha$ emission in T Tauri Stars

## Radiation induced by relativistic electrons during flares. An application to RY Tau.

Ana I. Gómez de Castro<sup>1,2</sup>, Anna Antonicci<sup>3</sup>, and Juan Carlos Vallejo<sup>1,2</sup>

<sup>1</sup> AEGORA Research Group - Joint Center for Ultraviolet Astronomy, Universidad Complutense de Madrid, Plaza de Ciencias 3, 28040 Madrid, Spain e-mail:

<sup>2</sup> Departamento de Física de la Tierra y Astrofísica, Fac. de CC. Matemáticas, Plaza de Ciencias 3, 28040 Madrid, Spain

<sup>3</sup> I.I.S. Enrico Fermi, Via Monte Nero, 15/A - 28041 Arona, Italy  
e-mail: aig@ucm.es \*

Received ; accepted

### ABSTRACT

*Context.* T Tauri Stars (TTSs) are magnetically active stars that accrete matter from the inner border of the surrounding accretion disc; plasma gets trapped into the large scale magnetic structures and falls onto the star, heating the surface through the so-called accretion shocks. The X-ray spectra of the TTSs show prominent Fe II  $K\alpha_{1,2}$  fluorescence emission at 6.4 keV (hereafter, Fe  $K\alpha$  emission) that cannot be explained in a pure accretion scenario since its excitation requires significantly more energy than the maximum available through the well constrained free-fall velocity. Neither, it can be produced by the hot coronal plasma.

*Aims.* TTSs display all signs of magnetic activity and magnetic reconnection events are expected to occur frequently. In these events, electrons may get accelerated to relativistic speeds and their interaction with the environmental matter may result in Fe  $K\alpha$  emission. It is the aim of this work to evaluate the expected Fe  $K\alpha$  emission in the context of the TTS research and compare it with the actual Fe  $K\alpha$  measurements obtained during the flare detected while monitoring RY Tau with the XMM-Newton satellite.

*Methods.* The propagation of high-energy electrons in dense gas generates a cascade of secondary particles that results in an electron shower of random nature whose evolution and radiative throughput is simulated in this work using the Monte Carlo code PENELOPE. A set of conditions representing the environment of the TTSs where these showers may impinge has been taken into account to generate a grid of models that can aid to the interpretation of the data.

*Results.* The simulations show that the electron beams produce a hot spot at the point of impact; strong Fe  $K\alpha$  emission and X-ray continuum radiation are produced by the spot. This emission is compatible with RY Tau observations.

*Conclusions.* The Fe  $K\alpha$  emission observed in TTSs could be produced by beams of relativistic electrons accelerated in magnetic reconnection events during flares.

**Key words.** stars: variables: T Tauri, stars: low-mass, accretion, stars: RY Tau

## 1. Introduction

Low mass pre-main sequence stars (PMS) are strongly magnetized sources with fields shaped in complex topologies (Villabrun et al. 2019; Yang & Johns-Krull 2011; Phan-Bao et al. 2009) that interact with the magnetized outflows launched from the accretion disc (Dyda et al. 2015; Kulkarni & Romanova 2013; Romanova et al. 2012). In the process, matter from the inner border of the disc gets trapped into large scale magnetic structures and falls onto the star, heating the surface through the so-called accretion shocks. X-ray emission is expected to be produced at the shock fronts and contribute to the overall X-ray radiation especially, in heavily accreting TTSs (Lamzin 1998; Kastner et al. 2002; Schmitt et al. 2005). TTSs also display an intense flaring activity that shows in the X-ray spectrum (Preibisch et al. 2005; Wolk et al. 2005; Favata et al. 2005; Tsujimoto et al. 2005).

The X-ray spectrum of the TTSs displays some prominent spectral features and, among them, a prominent Fe II  $K\alpha_{1,2}$  unresolved doublet at 6.4 keV (hereafter, the Fe  $K\alpha$  line), which

is observed during the flares and whose origin remains uncertain (Skinner et al. 2016; Tsujimoto et al. 2005; Czesla & Schmitt 2010). The Fe  $K\alpha$  emission cannot be explained by accretion since the excitation of the line requires significantly more energy than the maximum available through the well constrained free-fall velocity (Skinner et al. 2016; Günther & Schmitt 2008). Nor can it be produced by the hot coronal plasma in the stellar atmosphere; this plasma indeed, causes the broad blend of Fe XXV lines (6.5 keV-6.7 keV) (see, Phillips 2004, for details) often observed during flares in the Sun and other magnetic stars (including TTSs).

The excitation of the Fe  $K\alpha$  transition requires cold material, such as that present in the stellar photosphere or at the inner border of the accretion disc, that is excited by X-ray irradiation or by collisions with fast particles, resulting in the subsequent fluorescence emission at Fe  $K\alpha$ . In the flares observed on the Sun and on main-sequence stars the 6.4 keV line is usually much weaker than the 6.7 keV line as a result, it is expected that the Fe  $K\alpha$  excess of the TTSs is caused by the excitation of disc material. Previous work has addressed, the relevance of X-ray irradiation from the stellar corona in this process, but requires

\*

the irradiation of a large fraction of the disc surface to account for the observed flux, *i.e.* it requires that the disc is flared (Drake et al. 2008). However, there is not yet an evaluation addressing the relevance of fast particles collisions in the line excitation. This work addresses this issue.

In this work, we calculate the X-ray radiation produced by the interaction between the beams of relativistic electron (hereafter, e-beams) produced in the flares with the surrounding matter. Electrons are accelerated to relativistic speeds during magnetic reconnection. In the Sun, electrons may reach energies in the MeV range during the *impulsive phase* due to the onset of plasma micro-instabilities in the reconnection process (see *e.g.* Heyvaerts et al. (1977)). The impact of such relativistic e-beams in circumstellar structures, such as the inner border of the disc, or on the stellar surface generates a cascade of secondary particles that represents an effective degradation of the energy or shower which heats the environment and produces X-ray radiation. If the medium is dense enough, the propagation of the e-beams results in the generation of a hot spot at the impact point where most of the energy is released into heating. Otherwise, in low density media, the e-beam propagates releasing just a tiny fraction of its kinetic energy into the environment. As a result, the output X-ray spectra from the interaction of e-beams with a given medium depends strongly on the e-beam energy but also on the properties of the medium (and the view point, see Antonicci & Gómez de Castro 2005; Gómez de Castro & Antonicci 2006). It is the purpose of this work to compute a network of models that represent the expected X-ray signature of this interaction in the context of TTSs research.

This work is presented as follows. In Sect. 2, we describe the code and the general assumptions behind it. The impact of the e-beam in the surrounding medium results in a random shower of secondary electrons whose interaction with the environment is evaluated using a Monte Carlo code due to its random nature. For this purpose, we will use the PENELOPE code which is described in this section. In Sect. 3, a first set of simulations evaluating the output X-ray from the impact in uniform cloudlets is analyzed. In Sect. 4, the output radiation expected from the impact the e-beam on the inner border of the accretion disc described and in Sect. 5, these results are applied to the interpretation of the X-spectrum of RY Tau during the 2013 superflare (Skinner et al. 2016). The article concludes with a short summary of the main results (Sect. 6).

## 2. Numerical simulations and set-up

The simulations have been carried using the Monte Carlo code PENELOPE which requires the specification of the characteristics of an e-beam and the environment through which it propagates. In this section, we describe the PENELOPE code and its tuning to address the propagation of e-beam in the TTSs environment. We also describe, which are the characteristics of the e-beams considered. We defer for the followings sections the description of the two specific grids of simulations run for this investigation.

### 2.1. The Monte Carlo code PENELOPE

The propagation of a high-energy electrons in dense gas generates a cascade of secondary particles; after each interaction, the energy of the primary (or secondary) particle is reduced and, as a result, the evolution represents an effective degradation of the energy or shower; the energy is progressively deposited into the

medium and shared by an increasingly larger number of particles.

The evolution of an electron shower is of a random nature thus, the process is amenable to Monte Carlo simulation. The simulation of photon transport is straightforward since the mean number of events in each history is small. In practice, high energy photons are absorbed after a single photoelectric or pair-production interaction or after a few Compton interactions. The simulation of electron transport is much more difficult since the average energy loss by an electron in a single interaction is very small (around a few tens of eV). As a consequence, high-energy electrons suffer a large number of interactions before being effectively absorbed in the medium. Hence, detailed simulation is feasible only when the average number of collisions in the path is not too large.

For high-energy electrons, most of the Monte Carlo codes rely on multiple scattering theories which allow the simulation of the global effect of a large number of events in a track segment of a given length (or *step*). This procedure is referred to as “condensed” Monte Carlo method since the global effect of a large number of events is condensed in a single *step*.

In this work, we use the program developed by Antonicci (2004) to simulate the propagation of fast electrons in plasmas. This program runs a subroutine package named PENELOPE which is a Monte Carlo code<sup>1</sup> initially designed to study the propagation of electron-photon showers, with energy from 100 keV to several hundred MeV, in arbitrary materials, see Baró et al. (1994) and references therein. The cross sections for hard elastic scattering, hard inelastic collisions, hard bremsstrahlung emission, soft *artificial* events and positron annihilation are taken into account to calculate the interactions of the electrons with matter.

The following cross sections have been taken into account for the interaction of the secondary photons with the cloud: coherent (Rayleigh) scattering, incoherent (Compton) scattering, photoelectric absorption of photons and electron-positron pair production.

We have set a minimum energy threshold of 1 keV for the electrons since electrons with lower energy are not able to induce significant radiative effects in the X-ray range in the gas. The program is described in full detail in Antonicci (2004). It has also been adapted to simulate fast electron propagation in solid matter within the context of laser-matter interaction. This has allowed validating the collisional part of the code by comparing the computational results with the experimental results from LULI (Laboratoire pour l’utilisation de lasers intenses) and from the Livermore laboratory<sup>2</sup>.

<sup>1</sup> The Monte Carlo algorithm implemented in PENELOPE incorporates a “mixed” scattering model for the simulation of electron and positron transport. Hard interactions, with scattering angle and/or energy loss greater than preselected cutoff values are simulated in detail, by using simple analytical differential cross sections for the different interaction mechanisms and exact sampling methods. Soft interactions, with scattering angle or energy loss less than the corresponding cutoffs, are described by means of a multiple scattering approach. The code is user-friendly and incorporates photon cross-section data from the EPDL97 which includes new libraries for the low-energy photon cross-sections, such as XCOM and EPDL97. The code is available at the web site of the International Atomic Energy Agency (<http://www.nea.fr/lists/penelope.html>)

<sup>2</sup> The code is, in addition, widely used in the medical community and, for instance, Sung-Joon et al. (2004) have recently verified it for clinical dosimetry of high-energy (10 keV-150 keV) electron and photon beams.

## 2.2. The properties of the e-beam

In the context of the TTS research, the most luminous e-beams are accelerated in the reconnection events associated with strong flares. The X-ray light curves display a rich phenomenology of events; from compact flares similar to those observed in magnetically active stars, to extended flares proposed to be associated with large-scale loops that may reach about few stellar radii in length (see i.e. Favata et al. 2005) and would require average field strengths at the base of the corona of  $\sim 100 - 150$  kG (Jardine et al. 2006); the density of the plasma within these loops is  $10^{10} - 10^{11} \text{ cm}^{-3}$ .

A basic estimate of the expected mechanical luminosity of these strong e-beams can be obtained from the power needed to accelerate the particles ( $L$ ), which is roughly given by,

$$L = \frac{B^2}{8\pi} V_A \delta A = 0.85 \times 10^{30} \left(\frac{\text{erg}}{\text{s}}\right) \left(\frac{B}{100\text{G}}\right)^3 \left(\frac{n}{10^{10}\text{cm}^{-3}}\right)^{-0.5} \left(\frac{\delta A}{10^{19}\text{cm}^2}\right) \quad (1)$$

where  $B$ , is the magnetic field,  $\delta A$ , the section of the reconnecting current and,  $V_A$ , the Alfvén velocity of the plasma given by,

$$V_A = \frac{B}{(4\pi m_H n)^2} \quad (2)$$

and  $m_H$ , the mass of the Hydrogen atom and  $n$ , the particle density. The most uncertain parameter in this calculation is the surface of the reconnecting layer. For instance, for the super-flares described above, it seems reasonable to assume that magnetic reconnection occurs when the giant magnetic loop meets the inner border of the disc. Given the typical radius and the expected scale-height of the inner border of the disc (see Sect. 4), the surface of the re-connecting layer could be as large as  $\sim 10^{19} \text{ cm}^2$  and luminosity of the flare as high as  $2 \times 10^{-4} L_\odot$  (see Eq. 1). In practice, only a fraction of the magnetic energy released in the flare goes into particles acceleration; according to recent observations of Solar flares, this fraction is about  $\sim 50\%$  of the total energy (Battaglia et al. 2019).

However, this bulk luminosity is significantly smaller than the rise of the X-ray flux observed during flares in TTSs. For instance, the X-ray luminosities reach on average  $\langle L_X \rangle = 10^{32} \text{ erg s}^{-1}$  during strong flares but some events get as strong as  $L_X = 0.25 L_\odot$ ; see i.e. the event detected in AN Ori during the Chandra Orion Ultradeep Project (COUP) survey (Favata et al. 2005) or the flare detected with the ASCA satellite during the observation of V773 Tau (Tsuboi et al. 1998). Thus, given the uncertainties involved, we have opted to compute the expected X-ray spectrum for a set of e-beams with mechanical luminosities ranging from  $2 \times 10^{-4} L_\odot$  up to  $2 \times 10^{-1} L_\odot$ .

The energy distribution of the electrons in the beam can be modelled by a power law (see Oka et al. 2008, for an in-depth discussion). In particular, the distribution function of the number of electrons ( $n_e$ ) per kinetic energy ( $\epsilon$ ) is often described, as a single power law with index -4. For our application, the distribution could be truncated to energies between 30 keV and 2 MeV:

$$n(\epsilon) \propto \epsilon^{-4}, \quad \text{for } 30\text{keV} \leq \epsilon \leq 10\text{MeV} \quad (3)$$

The low energy cut-off is set to disregard the contribution of low energy electrons since they produce optically thin Bremsstrahlung radiation and no Fe  $K\alpha$  emission. The upper threshold is set to optimize the computation time of the simulations. This limit guarantees reaching an accuracy of  $10^{-4}$  in

the total energy, which is more than enough for the the accuracy of the X-ray observations of the TTSs (and the purpose of this work).

Using a power law distribution presents however, some drawbacks for the diagnoses intended in this work. In particular, the mean kinetic energy of the electrons ( $\langle K \rangle$ ) cannot be tuned to evaluate to what extent is significant in the output Fe  $K\alpha$  emission. For this reason, we have opted for a Maxwell relativistic (MR) distribution and worked with e-beams of different mean kinetic energies. The mathematical form of the distribution function of the number of electrons ( $n_e$ ) with the kinetic energy ( $K$ ) and is given by,

$$\frac{dn_e}{dK} = \gamma(\gamma^2 - 1)^{1/2} e^{-K/k_B T_e} \quad (4)$$

with  $\gamma = (1 - (v/c)^2)^{-1/2}$  and  $K = 0.511 \text{ MeV}(\gamma - 1)$ ;  $k_B$  is the Boltzmann constant and  $T_e$ , the electron temperature. Note that the mean kinetic temperature of the e-beam is  $\sim 3k_B T_e$  since the distribution has a broad tail toward high energies.

Finally, the e-beam is assumed to have cylindrical symmetry and the electrons be distributed within any given section following a radial distribution such that,

$$n_e(r) = n_{e,0} \exp\left(-\left(\frac{r}{r_0}\right)^2\right) \quad (5)$$

with  $r_0 = 10^5 \text{ cm}$ . The value of  $n_{e,0}$  is set to satisfy the injection of the total mechanical luminosity in 100 s.

## 3. Basic simulations: propagation through an homogeneous medium

This grid of simulations has been run to characterize the radiative output produced at X-ray wavelengths (2-30 keV) by the propagation of an e-beam through a uniform density medium. The medium includes the most abundant elements up to Iron in solar abundance (Anders & Ebihara 1982). In this set-up, the e-beam impinges perpendicularly to the surface of the medium which is a spherical cloudlet of uniform density and diameter  $10^{10} \text{ cm}$ . The simulations have been run for cloudlet densities ranging from  $10^9 \text{ cm}^{-3}$  to  $10^{17} \text{ cm}^{-3}$  in powers of ten. The lower limit is set by the density of the accreting matter trapped in the funnel flows that channel the gas from the disc onto the stellar surface; ultraviolet observations of the semi-forbidden C II] emission at  $2323 \text{ \AA}$  indicate that the density ranges from  $10^9 \text{ cm}^{-3}$  to  $10^{12} \text{ cm}^{-3}$  in these structures (López-Martínez & Gómez de Castro 2014). The upper limit is set for the expected mid-plane density at the innermost border of an accretion disk around a solar mass TTS undergoing an accretion rate of  $10^{-6} M_\odot \text{ yr}^{-1}$  (see Sect 2.5).

The mechanical luminosity of the e-beam is  $0.002 L_\odot$  and  $\langle K \rangle$  values of 200 keV, 400 keV, 800 keV and 1.6 MeV have been tested. In all cases, an MR energy distribution has been assumed for the electrons in the e-beam.

The e-beam propagation results in the production of X-ray radiation. We have measured the backscattered and forward scattered radiation from the cloudlet along the direction of propagation of the e-beam. A hot spot is always produced at the entry point however, to observe X-ray radiation from the back, the density of the medium needs to be  $\leq 10^{14} \text{ cm}^{-3}$ . Note that X-ray radiation is fully absorbed for column densities above  $10^{24} \text{ cm}^{-2}$  (Morrison & McCammon 1983). The characteristics of the output X-ray spectra are summarized in Fig. 1 and some sample spectra are shown in Fig. 2 and Fig. 3 for the rear of the cloudlet

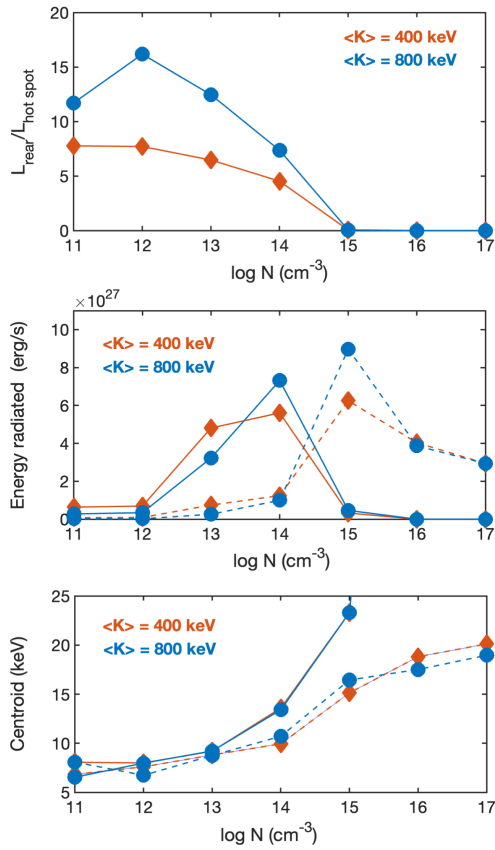


**Fig. 1.** General properties of the X-ray spectrum for beam  $K= 400$  keV (red) and  $K = 800$  keV (blue). Top: ratio between the luminosity radiated from the rear of the cloud and the hot spot, at the front, as a function of the density of the cloud. Middle: Luminosity of the spectra as a function of the density. Bottom: dependence of the centroid of the X-ray energy distribution on the cloud density. The continuous and dashed lines refer to data from the transmitted and back-scattered spectra. The kinetic energy of the e-beam is fully absorbed within the cloud for particle densities above  $10^{14}$  cm<sup>-3</sup>.

and the back-scattered radiation from the hot spot, respectively. In general, the spectra are harder, *i.e.*, the centroid of the X-ray energy distribution is observed at higher energies, as the density of the cloud increases. Increasing the mean kinetic energy of the e-beam has the same effect.

The spectrum of the hot spot contains some additional interesting features including some prominent emission lines. The Fe  $K\alpha$  line (6.4 keV) is observed for  $N > 10^{13}$  cm<sup>-3</sup>, as a strong feature in the spectrum; this line is actually, an unresolved doublet produced in the transitions  $[1s2S^{1/2}] - [2p2P^{1/2,3/2}]$  of Fe II. For e-beams with kinetic energy,  $K \geq 800$  MeV and  $N \geq 10^{16}$  cm<sup>-3</sup>, also the Fe  $K\beta$  line at 7.1 keV is observed. As shown in Fig. 4, the strength of the Fe  $K\alpha$  line decreases as the density of the cloud increases while the strength of the Fe II  $K\beta$  line depends on the energy of the e-beam; also, the ratio Fe  $K\alpha$ /Fe  $K\beta$  decreases with the energy of the beam. The broad iron feature at  $\sim 6.7$  keV, which is usually observed in TTSSs, only shows in few spectra (see Fig. 5); this feature arises from very hot plasma in the hot spot at the point of impact of the e-beam. This Fe XXV feature is probably a blend of the x, y, and z lines of Fe XXV (see Phillips 2004, for a detailed description of the main transitions).

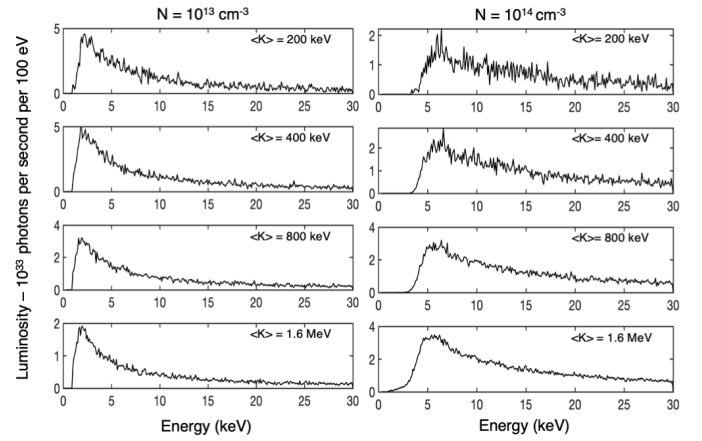


**Fig. 2.** Output X-ray spectrum from the rear of the cloud.

To summarize, the main features derived from this grid of simulations are:

- Fe  $K\alpha$  (and  $K\beta$ ) emission is only observed in the spectra of the hot spot and for densities above  $10^{14}$  cm<sup>-3</sup>.
- $\langle K \rangle \geq 400$  keV maximizes the Fe  $K\alpha$  emission (see Fig. 5).
- Increasing  $\langle K \rangle$  or increasing the density of the clouddlet shifts the centroid, *i.e.* makes the output X-ray spectrum harder.

In general, this process is inefficient in terms of the X-ray radiation production compared with the input of mechanical energy of the e-beam. As an example, in the simulation with  $\langle K \rangle = 400$  keV and  $N = 10^{14}$  cm<sup>-3</sup>, the hot spot radiates (in the 2 - 30 keV) range only  $\sim 0.07\%$  of the input mechanical luminosity of the e-beam and the radiation from the rear of the clouddlet is ten times smaller. Most of the energy is diffuse away of the clouddlet by the scattered electrons and thus, only large dense structures are efficient in the transference of the e-beam energy into X-ray radiation.

#### 4. X-ray output from the impact of e-beams on the accretion disc

In this set-up, the e-beam is assumed to impinge perpendicularly to the surface of the disk, which is stratified. The disc is modelled as a set of plane parallel layers of increasing density to the mid-plane following the vertical structure of a standard  $\alpha$  disc (Shakura & Sunyaev 1973); the scalings have been adopted from Gómez de Castro (2013). The e-beam impacts on the disc from the  $z$  axis, as shown in Fig. 6, and the disc density depends on  $z$  as,

$$\rho(R, z) = \rho(R, 0) \exp\left(-\frac{z^2}{2H^2}\right) \quad (6)$$

with,

$$H(R) = 3.4 \times 10^9 \text{ cm} \left(\frac{\dot{M}}{10^{-8} M_{\odot} \text{ yr}^{-1}}\right)^{1/8} \cdot \left(\frac{M}{M_{\odot}}\right)^{-3/8} \left(\frac{R}{0.014 \text{ AU}}\right)^{9/8} \quad (7)$$

and,

$$\rho(R) = 0.94 \times 10^{-8} \text{ g cm}^{-3} \left(\frac{\dot{M}}{10^{-8} M_{\odot} \text{ yr}^{-1}}\right)^{5/8} \left(\frac{M_*}{0.5 M_{\odot}}\right)^{5/8} \left(\frac{R}{0.014 \text{ AU}}\right)^{-15/8} \quad (8)$$

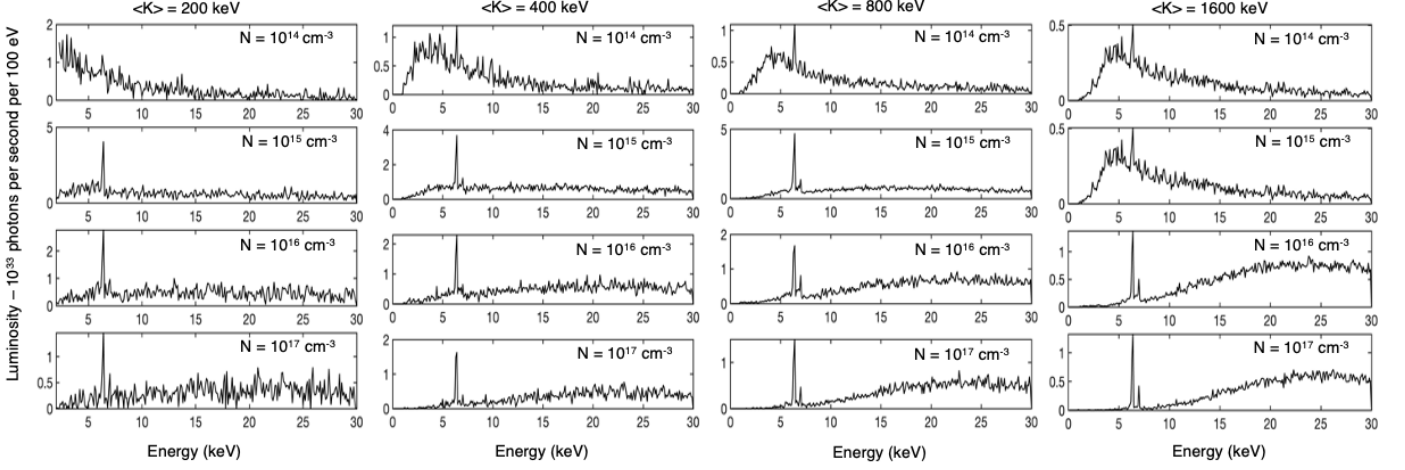


**Fig. 3.** Output X-ray spectrum from the hot spot obtained for kinetic energies of the e-beam: 200 keV, 400 keV, 800 keV, 1.6 MeV (see top) and media density:  $10^{14} \text{ cm}^{-3}$ ,  $10^{15} \text{ cm}^{-3}$ ,  $10^{16} \text{ cm}^{-3}$ , and  $10^{17} \text{ cm}^{-3}$ . No hot spot is produced for the lowest simulated density  $N = 10^{13} \text{ cm}^{-3}$ , neither Fe  $K\alpha$  emission.

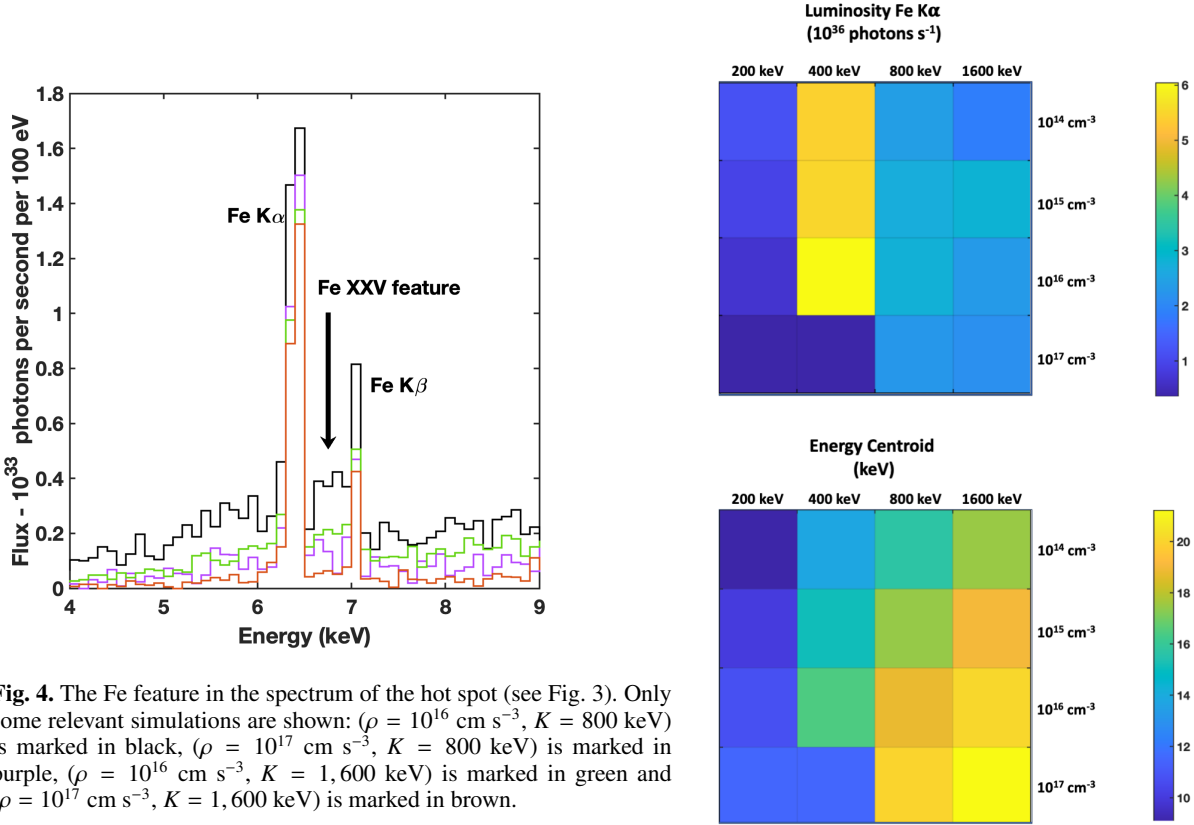


**Fig. 4.** The Fe feature in the spectrum of the hot spot (see Fig. 3). Only some relevant simulations are shown: ( $\rho = 10^{16} \text{ cm s}^{-3}$ ,  $K = 800 \text{ keV}$ ) is marked in black, ( $\rho = 10^{17} \text{ cm s}^{-3}$ ,  $K = 800 \text{ keV}$ ) is marked in purple, ( $\rho = 10^{16} \text{ cm s}^{-3}$ ,  $K = 1,600 \text{ keV}$ ) is marked in green and ( $\rho = 10^{17} \text{ cm s}^{-3}$ ,  $K = 1,600 \text{ keV}$ ) is marked in brown.

The disc temperature is given by,

$$T(R) = 1,765K \left( \frac{\dot{M}}{10^{-8} M_{\odot} \text{ yr}^{-1}} \right)^{1/4} \left( \frac{M_{*}}{0.5 M_{\odot}} \right)^{1/4} \left( \frac{R}{0.014 \text{ AU}} \right)^{-3/4} \quad (9)$$

The PENELOPE numerical code is not designed to work with a density profile along the z-axis of the irradiated sample. To overcome this problem, the disc has been implemented as set of plane parallel layers of uniform density. The exponential profile described in Eq 5 is reproduced by 10 layers, as shown in Fig. 6 and the mean density changes by a  $\sim 25\%$  between layers.

**Fig. 5.** Variation of the Fe  $K\alpha$  flux (top) and the energy centroid (bottom) of the X-ray spectrum with the cloud density and the mean kinetic energy of the beam  $\langle K \rangle$ .

The grid of simulations is summarized in Table 1. As in Sect. 3, the radius of the e-beam is assumed to be  $10^5 \text{ cm}$  and the disc composition is set to solar abundances. The output spectra obtained for an e-beam with  $\langle K \rangle \geq 800 \text{ keV}$  are represented in Figs.7 (transmitted) and 8 (hot spot). For the range of mechanical luminosities of the e-beam studied in this work

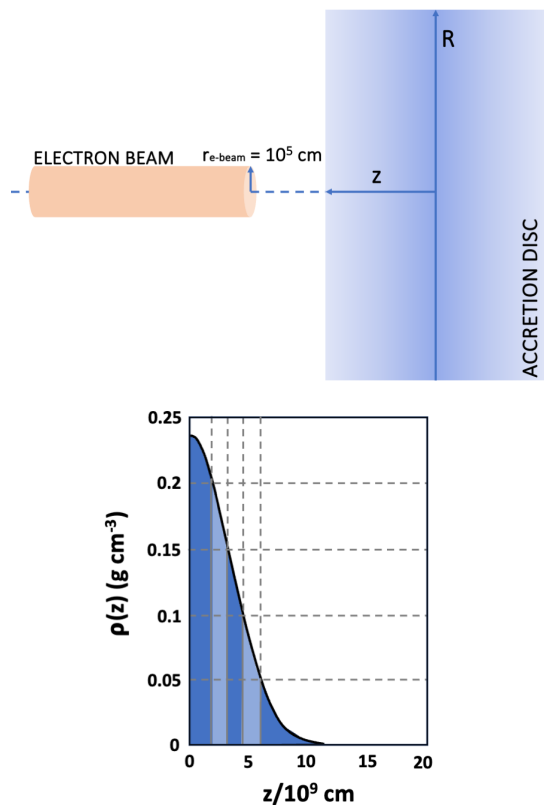


**Fig. 6.** Top: Simulation scheme. The e-beam impinges normally on the accretion disc surface. Bottom: The normalized density profile (see Eq. 6) is represented for the inner border of a sample disc with accretion rate  $10^{-8} M_{\odot} \text{yr}^{-1}$ . The structure is symmetric around the disc mid-plane and only the upper part is represented. The density profile from Eq. 6 is plotted with a blue line and the limits of the five layers implemented in the simulation are marked with dashed lines.

**Table 1.** Network of simulations of the interaction of the e-beams with the inner disc \*

Simulation Id.	Properties of the disc <sup>1</sup>			
	Acc. Rate ( $M_{\odot} \text{yr}^{-1}$ )	$H_0$ (cm)	$T_0$ (K)	$\rho_0$ ( $g \text{cm}^{-3}$ )
AD-Ma6	$10^{-6}$	$6.1 \times 10^9$	5,581	$1.7 \times 10^{-7}$
AD-Ma7	$10^{-7}$	$4.5 \times 10^9$	3,139	$3.9 \times 10^{-8}$
AD-Ma8	$10^{-8}$	$3.4 \times 10^9$	1,765	$9.4 \times 10^{-9}$
AD-Ma9	$10^{-9}$	$2.5 \times 10^9$	993	$2.2 \times 10^{-9}$
AD-Ma10	$10^{-10}$	$1.9 \times 10^9$	558	$5.3 \times 10^{-10}$
AD-Ma11	$10^{-11}$	$1.4 \times 10^9$	314	$1.2 \times 10^{-10}$

<sup>1</sup>  $H_0$ ,  $T_0$ ,  $\rho_0$  are computed for the mid-plane at  $R_0$  for the given accretion rate (Eq. 7-9).

( $\sim 10^{-1} - \sim 10^{-4} L_{\odot}$ ), the X-ray luminosity increases linearly with the e-beam mechanical luminosity thus, only spectra corresponding to a sample luminosity ( $2 \times 10^{-3} L_{\odot}$ ) are represented in the figures.

As expected, the e-beam is absorbed in high density environments; this translates into accretion rates  $M_a > 10^{-10} M_{\odot} \text{yr}^{-1}$  in the accretion disc scenario. The transmitted spectrum is only observed for the most rarified accretion discs and the cut-off energy shifts to higher energies as the accretion rate increases (see Fig.

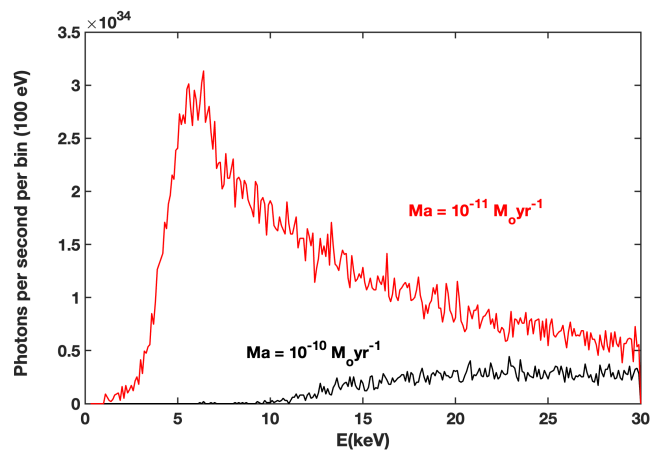


**Fig. 7.** Transmitted X-ray spectrum. Simulation with e-beam luminosity:  $2 \times 10^{-3} L_{\odot}$ .

7). Again, no spectral features are observed in the transmitted spectrum.

The spectrum of the hot spot displays a prominent Fe  $K\alpha$  feature and X-ray continuum emission whose properties depend on the accretion rate, *i.e.* on the density and stratification of the disc (see Fig. 8).

To study the dependence of the spectrum with the e-beam energy, an additional set of simulations has been run for an accretion rate of  $10^{-7} M_{\odot} \text{yr}^{-1}$  and  $\langle K \rangle = 40, 100, 200, 400, 800, 1600$  KeV. As expected, as the e-beam mean kinetic energy rises, the Fe feature becomes stronger and the centroid of the back-scattered spectrum moves to higher energies.

The trends described in this section can be summarized as follows,

- Fe  $K\alpha$  (and  $K\beta$ ) emission is very weak or absent in the transmitted spectra.
- Increasing the mean kinetic energy ( $\langle K \rangle$ ) of the e-beam or increasing the density of the medium shifts the centroid of the spectrum to higher energies.

Also the e-beam is highly directive, the size of the hot spot at the point of impact is comparable to the beam radius and the radiative output scales linearly with the surface of spot.

## 5. Interpretation of RY Tau flares

RY Tau is among the best studied accreting TTSs at X-rays. Its X-ray spectrum is known to vary from quiescence to flare state from the observations carried out with the Chandra and the XMM-Newton satellites (see Skinner et al. 2016). For this work, we will use the XMM-Newton observations to evaluate whether the reported Fe  $K\alpha$  emission during flares can be produced from the hot spots generated during the flares.

RY Tau was observed in September 2000 and in August 2013 (see Table 2) however, no significant flaring activity was detected in 2000 (Güdel et al. 2007). We have retrieved the data obtained with the European Photon Imaging Camera (EPIC) pn instrument in 2013 from the archive, id. 0722320101, and processed them using the XMM-Newton Science Analysis System (SAS 19.0.0). Spectrum analysis was done using XSPEC 12.11.1.

Following an approach similar to Skinner et al. (2016), the spectra have been extracted using PN cleaned and filtered for

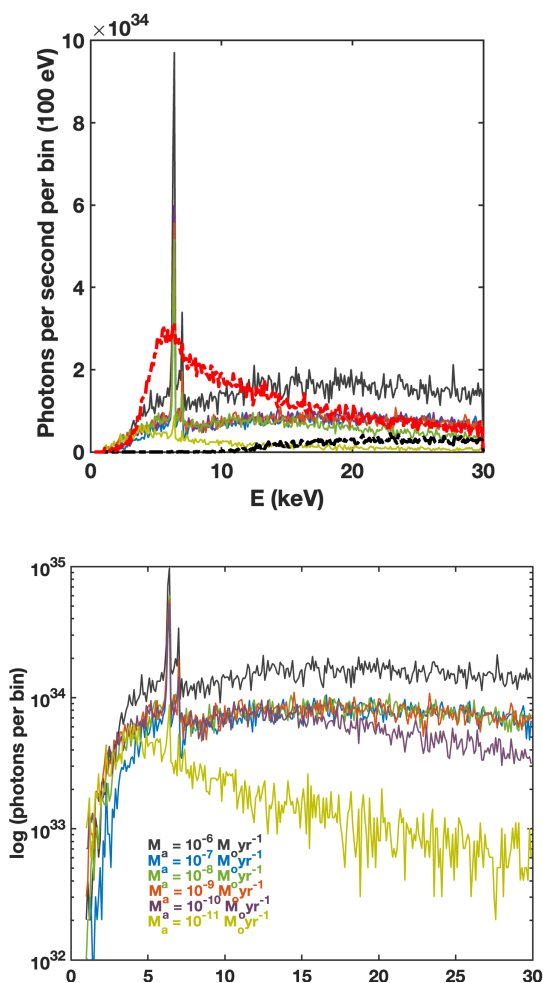


**Fig. 8.** Output X-ray spectrum of the hot spot. *Top panel:* Comparison between the X-ray spectra of the hot spot (thin lines) with the transmitted spectra (thick dashed lines, see Fig. 7). All the spectra are plotted in the same scale. Note the strength of the Fe feature in the back-scattered spectrum at high accretion rates. *Bottom panel:* X-ray spectra of the hot spot in logarithmic scale. E-beam properties:  $K = 800 \text{ keV}$  and  $2 \times 10^{-3} L_\odot$ . All the spectra are plotted at the same scale.

**Table 2.** XMM-Newton EPIC observations of RY Tau

Observation ID.	Start date of observation dd - mm - yyyy hh:mm:ss	Duration (s)
0101440701	05-09-2000 02:08:06	51,315
0722320101	21-08-2013 04:16:33	112,600

background event files. Firstly, the event files were created by removing high energy protons intervals at the end of the exposure and by time-filtering for covering the quiescent and flare periods. The quiescent spectrum was produced using events from 0.0 to 20.0 ks and from 45.0 to 90.0 ks, and the flare spectrum using events from 20.0 to 45.0 ks. Then, source and background spectra were extracted using the *evselect* task. After that, the source spectra were obtained using a computed redistribution matrix and the proper ancillary file. Finally, the spectra were rebinned using the *specgroup* task. The quiescent spectrum was rebinned in order to have at least 40 counts for each background-subtracted spectral channel. The flare spectrum was then rebinned to group it in exactly the same way as the source spectrum. They are plot-

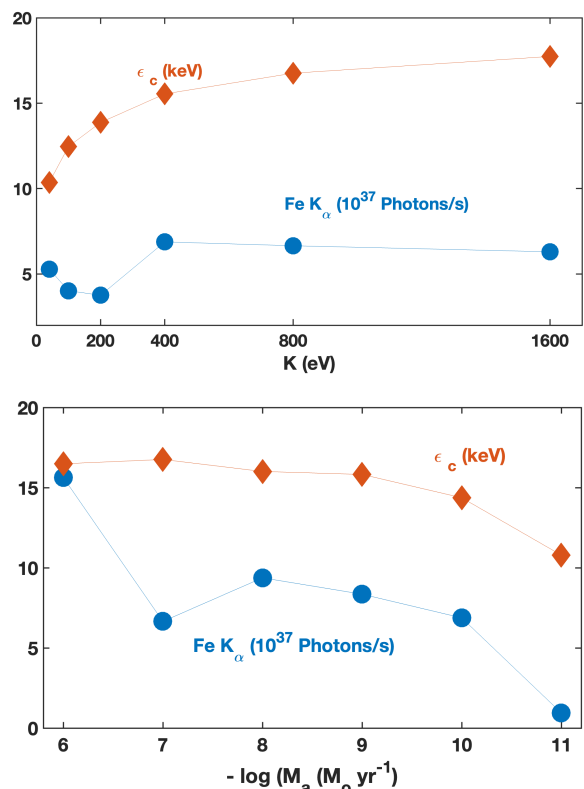


**Fig. 9.** Variation of the centroid of the X-ray spectrum and the Fe K $\alpha$  flux with: *top* the average energy of the e-beam (for  $M_a = 10^{-7} M_\odot \text{yr}^{-1}$ ), and, *bottom* the accretion rate (for  $K=800 \text{ keV}$ ).

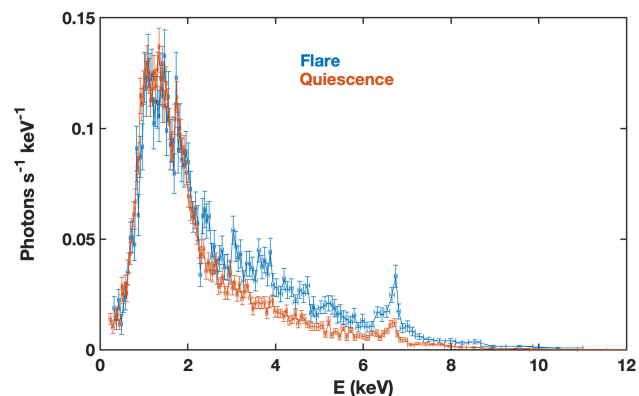


**Fig. 10.** X-ray spectrum of RY Tau obtained with the instrument EPIC on board the XMM-Newton satellite in August, 2013 (observation ID: 0722320101). The X-ray light curve has been analyzed to discriminate the flare spectrum from the quiescence one.

ted in Figure 10 and are similar to those in Fig. 3 of Skinner et al. (2016).

During the flare, the X-ray flux increases at energies above 2 keV; the prominent Fe K $\alpha$  emission is also, clearly apparent as well as the Fe XXV feature. The spectral energy distribution of the X-ray emission during the flare is represented in Fig. 11. To obtain it, the quiescence spectrum is subtracted out from the flare spectrum but only energy bins with  $\text{SNR} \geq 3$  have been considered. The error bars have been computed using the standard expression for the linear propagation of errors:

$$\sigma_{\text{excess}}^2 = \sigma_{\text{flare}}^2 + \sigma_{\text{quiescence}}^2 \quad (10)$$

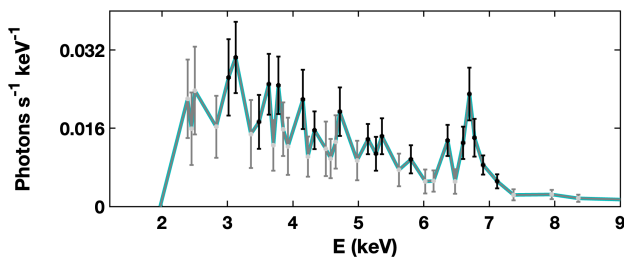


**Fig. 11.** Spectral distribution of the X-ray radiation produced by the flare. Data points with  $\text{SNR} \geq 3$  are marked in black and those with  $\text{SNR} \geq 2$  in grey. The green line is plotted to guide the eye to the overall energy distribution where the prominent Fe  $K\alpha$  and Fe XXV features are readily recognized.

with  $\sigma_{flare}$  and  $\sigma_{quiescence}$  the variances of the flare and quiescence spectra provided by XSPEC (for obvious reasons, some data points have  $\sigma_{excess} < 3$ ).

The Fe  $K\alpha$  flux during the flare has been computed using the XPEC routines and found to be:  $0.87 \times 10^{-13} \text{ erg s}^{-1} \text{ cm}^{-2}$ , which accounts to a total luminosity of the line of  $2.01 \times 10^{29} \text{ erg s}^{-1}$ , using the *Gaia* parallax of RY Tau (7.2349 mas) for the calculation. This luminosity is equivalent to a grand total of  $1.96 \times 10^{37}$  Fe  $K\alpha$  photons per second during the flare. This value should be divided by  $4\pi$  to compare it with the results from the simulations described in the previous sections.

This luminosity cannot be accounted by the impact of relativistic electrons on the diffuse environment around the loops (either the funnel flows or the dense stellar corona) since, as shown in Sect. 3, Fe  $K\alpha$  radiation is only produced if the density is very high ( $> 10^{14} \text{ cm}^{-3}$ ). However, the observed Fe  $K\alpha$  emission could arise from hot spots on the accretion disc generated at the impact point of the e-beams from the flares.

The environment around an active TTS such as RY Tau is strongly magnetized and has a complex topology prone to produce magnetic reconnection in many different regions. A simplified approach to the overall topology is displayed in Fig. 12 (after Gómez de Castro et al. 2016); the magnetic field is represented by solid lines with the very thick line marking the connection between the star and the inner border of the disc. In the classical TTS evolutionary state, the stellar field is connected with the disc field to the point that stellar rotation is locked to the Keplerian velocity of the inner border of the disc. The dashed lines mark the limit between the disc-dominated and the star-dominated regions. Over this magnetic sketch, the results of numerical simulations dealing with this interaction (Gómez de Castro & von Rekowski 2011) are shown in the figure; the green-brown shadowed regions are locations where magnetic reconnection occurs heating the gas and producing ultraviolet radiation. In this environment, the most obvious region to have frequent and strong reconnection events is the inner border of the disc. However, the geometry is not clear; reconnection may occur above the disc producing e-beams impacting on the disc surface (as simulated in Sect. 4) however, e-beams may be generated just at the inner border and interact with specific layers of the disc vertical structure. These two simple possibilities are marked in Fig. 12 as Option A and B, respectively. Though the geometry is going to be much more complex in general, let us keep simple for this prospective work and evaluate whether the Fe  $K\alpha$  emission detected during the flare is compatible with the radiation produced

in the propagation of the high energy e-beams produced during large flares within the disc.

According to the simulations in Sect. 4, the Fe  $K\alpha$  luminosity produced by an e-beam impacting perpendicularly to the accretion disc depends on the accretion rate which has been measured to range between  $0.91 \times 10^{-7} M_{\odot} \text{ yr}^{-1}$  and  $0.50 \times 10^{-7} M_{\odot} \text{ yr}^{-1}$  for RY Tau (Alcalá et al. 2021). For these rates, the predicted line luminosity ranges between  $3.4 \times 10^{37}$  photons  $\text{s}^{-1}$  and  $4.7 \times 10^{37}$  photons  $\text{s}^{-1}$  for a mechanical luminosity of the e-beam of  $0.1 L_{\odot}$ , which is within a factor of two of the detected values. This factor could be easily accommodated reducing the luminosity of the flare or the surface of the hot spot.

In the case of a lateral impact (option B in Fig 12), the particle density of the mid-plane is expected to range between  $0.77 \times 10^{16} \text{ cm}^{-3}$  and  $1.13 \times 10^{16} \text{ cm}^{-3}$  (see Eq. 8) and thus, according to Fig. 5, the Fe  $K\alpha$  emission is predicted to range between  $3 \times 10^{36}$  photons  $\text{s}^{-1}$  and  $6 \times 10^{36}$  photons  $\text{s}^{-1}$  depending of the mean kinetic energy of the electrons, for an e-beam of mechanical luminosity of  $0.02 L_{\odot}$ . Since, the Fe  $K\alpha$  luminosity scales linearly with the mechanical luminosity, a strong flare with a luminosity  $0.1 L_{\odot}$  could produce an emission similar to the observed.

In summary, the Fe  $K\alpha$  emission detected in RY Tau during the large flare in 2013 can be easily accounted by the propagation of the e-beams generated during the flare within the inner border of the disc.

## 6. Conclusions

The X-ray observations of the TTSs have shown that some classical TTSs experience very strong flares which are associated with the release of magnetic energy during the reconnection of very long magnetic loops, extending few stellar radii. This strong reconnection events are possibly produced when stellar loops meet the inner of the disc. A characteristic of these flares is the detection of Fe  $K\alpha$  emission which, in the case of RY Tau, reaches a line luminosity of  $1.96 \times 10^{37}$  Fe  $K\alpha$  photons  $\text{s}^{-1}$  during the flare. In this work, we have shown that this emission can be naturally explained by the X-ray radiation produced at the impact point of the high energy electrons released during the reconnection event on the accretion disc.

This work also includes a broad network of numerical simulations of the expected X-ray radiative output in this context to aid the interpretation of X-ray observations of TTSs during flares.

This work has concentrated in modelling the radiative output from large flares meeting the inner border of the disc but similar phenomena (and Fe  $K\alpha$  emission) could be produced by the impact of the e-beams on the stellar surface however, in all cases, very strong flare luminosities are required to reproduce the observed Fe  $K\alpha$  flux.

*Acknowledgements.* This work has been partially funded by the Ministry of Science, Innovation and Universities of Spain through the grant with reference: PID2020-116726RB-I00.

## References

- Alcalá, J. M., Gangi, M., Biazzo, K., et al. 2021, A&A, 652, A72
- Anders, E. & Ebihara, M. 1982, Geochim. Cosmochim. Acta, 46, 2363
- Antonucci, A. 2004, PhD tesis, Universidad Complutense de Madrid
- Antonucci, A. & Gómez de Castro, A. I. 2005, A&A, 432, 443
- Baró, J., Sempau, J., Fernandez-Varea, J., & Salvat, F. 1994, Nucl. Instr. and Meth., B84
- Battaglia, M., Kontar, E. P., & Motorina, G. 2019, ApJ, 872, 204



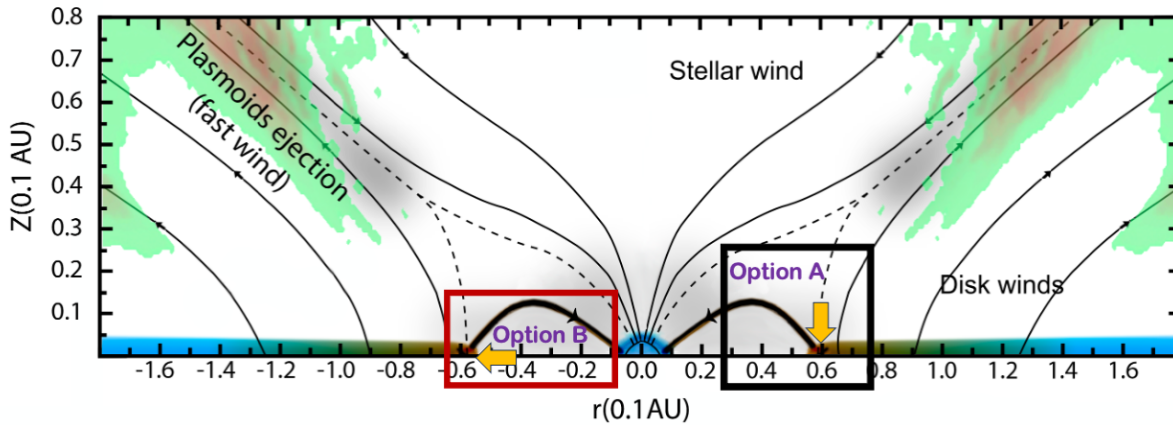


**Fig. 12.** Map of the C III] (191 nm) emissivity caused by the star-disc interaction from MHD simulations of the disc-star interaction (Gómez de Castro & von Rekowski 2011). On top, the main components of the TTSs environment and magnetic structure; stellar interaction with the infalling magnetized plasma drives the outflow and generates reconnection layers (dashed lines).

- Czesla, S. & Schmitt, J. H. M. M. 2010, *A&A*, 520, A38  
 Drake, J. J., Ercolano, B., & Swartz, D. A. 2008, *ApJ*, 678, 385  
 Dyda, S., Lovelace, R. V. E., Ustyugova, G. V., et al. 2015, *MNRAS*, 450, 481  
 Favata, F., Flaccomio, E., Reale, F., et al. 2005, *ApJS*, 160, 469  
 Gómez de Castro, A. I. 2013, in *Planets, Stars and Stellar Systems. Volume 4: Stellar Structure and Evolution*, ed. T. D. Oswalt & M. A. Barstow, Vol. 4, 279  
 Gómez de Castro, A. I. & Antonucci, A. 2006, *Astronomische Nachrichten*, 327, 989  
 Gómez de Castro, A. I., Gaensicke, B., Neiner, C., & Barstow, M. A. 2016, *Journal of Astronomical Telescopes, Instruments, and Systems*, 2, 041215  
 Gómez de Castro, A. I. & von Rekowski, B. 2011, *MNRAS*, 411, 849  
 Güdel, M., Briggs, K. R., Arzner, K., et al. 2007, *A&A*, 468, 353  
 Günther, H. M. & Schmitt, J. H. M. M. 2008, *A&A*, 481, 735  
 Heyvaerts, J., Priest, E. R., & Rust, D. M. 1977, *ApJ*, 216, 123  
 Jardine, M., Collier Cameron, A., Donati, J. F., Gregory, S. G., & Wood, K. 2006, *MNRAS*, 367, 917  
 Kastner, J. H., Huenemoerder, D. P., Schulz, N. S., Canizares, C. R., & Weintraub, D. A. 2002, *ApJ*, 567, 434  
 Kulkarni, A. K. & Romanova, M. M. 2013, *MNRAS*, 433, 3048  
 Lamzin, S. A. 1998, *Astronomy Reports*, 42, 322  
 López-Martínez, F. & Gómez de Castro, A. I. 2014, *MNRAS*, 442, 2951  
 Morrison, R. & McCammon, D. 1983, *ApJ*, 270, 119  
 Oka, M., Fujimoto, M., Nakamura, T. K. M., Shinohara, I., & Nishikawa, K. I. 2008, *Phys. Rev. Lett.*, 101, 205004  
 Phan-Bao, N., Lim, J., Donati, J.-F., Johns-Krull, C. M., & Martín, E. L. 2009, *ApJ*, 704, 1721  
 Phillips, K. J. H. 2004, *ApJ*, 605, 921  
 Preibisch, T., Kim, Y.-C., Favata, F., et al. 2005, *ApJS*, 160, 401  
 Romanova, M. M., Ustyugova, G. V., Koldoba, A. V., & Lovelace, R. V. E. 2012, *MNRAS*, 421, 63  
 Schmitt, J. H. M. M., Robrade, J., Ness, J. U., Favata, F., & Stelzer, B. 2005, *A&A*, 432, L35  
 Shakura, N. I. & Sunyaev, R. A. 1973, *A&A*, 24, 337  
 Skinner, S. L., Audard, M., & Güdel, M. 2016, *ApJ*, 826, 84  
 Sung-Joon, Y., Brezovich, I., Pareek, P., & Naqvi, S. 2004, *Phys. Med. Biol.*, 49  
 Tsuboi, Y., Koyama, K., Murakami, H., et al. 1998, *ApJ*, 503, 894  
 Tsujimoto, M., Feigelson, E. D., Grosso, N., et al. 2005, *ApJS*, 160, 503  
 Villebrun, F., Alecian, E., Hussain, G., et al. 2019, *A&A*, 622, A72  
 Wolk, S. J., Harnden, F. R., J., Flaccomio, E., et al. 2005, *ApJS*, 160, 423  
 Yang, H. & Johns-Krull, C. M. 2011, *ApJ*, 729, 83